

Robust uncalibrated visual stabilization for nonholonomic mobile robots

Yao Huang & Jianbo Su

To cite this article: Yao Huang & Jianbo Su (2020) Robust uncalibrated visual stabilization for nonholonomic mobile robots, *Advanced Robotics*, 34:6, 388-399, DOI: [10.1080/01691864.2020.1717993](https://doi.org/10.1080/01691864.2020.1717993)

To link to this article: <https://doi.org/10.1080/01691864.2020.1717993>



View supplementary material [↗](#)



Published online: 23 Jan 2020.



Submit your article to this journal [↗](#)



Article views: 134



View related articles [↗](#)



View Crossmark data [↗](#)

FULL PAPER



Robust uncalibrated visual stabilization for nonholonomic mobile robots

Yao Huang  and Jianbo Su

Department of Automation, Shanghai Jiao Tong University, Shanghai, People's Republic of China

ABSTRACT

This paper proposes a new image-based visual servoing scheme for stabilizing the nonholonomic mobile robot equipped with a monocular vision system to the desired configuration. In the vision system, neither intrinsic nor extrinsic camera parameters are calibrated. In addition, the lack of depth information should be tackled when using a monocular camera. The main difficulty encountered lies in the simultaneous existence of nonholonomic constraints, uncalibrated camera parameters and unknown depth. To deal with these problems, a dual-loop control structure is utilized. For the inner loop, an extended state observer is constructed to observe the system uncertainties caused by the uncalibrated camera parameters and unknown depth. For the outer loop, a switching controller is synthesized based on the compensated system model to maneuver the mobile robot to the desired configuration. Simulations and experimental results illustrate the effectiveness and robustness of the proposed control scheme.

ARTICLE HISTORY

Received 3 July 2019
Revised 29 November 2019
Accepted 9 January 2020

KEYWORDS

Nonholonomic mobile robots; uncalibrated visual servoing; stabilization; extended state observer

1. Introduction

Mobile robot control and navigation have attracted a large number of researches over the last decades for its great contribution in applications [1]. However, wheeled mobile robots suffer from the dead-reckoning problem caused by the internal sensor such as wheel odometry. Simultaneous localization and mapping is such a methodology to simultaneously build a map of an unknown environment and determine the location within the map via observing the external landmarks, which means it can provide a more accurate pose estimation of the mobile robot than the internal sensor [2,3]. Full states can be used for mobile robot control and navigation, which is classified as the map-based methods [4–6]. Nevertheless, the map needs to be computed and maintained, which is wasteful in terms of memory to storing feature descriptors. In addition, the control performance of these methods is strictly dependent on the accuracy of the map given a priori and the map-based methods even fail in unexplored environments.

There is another methodology that directly uses an external visual sensor to obtain the visual information and performs the feedback control. One class of the methods is named as appearance-based or qualitative navigation, which does not build maps in advance. The path to be followed in the navigation is defined as a

pre-record sequence of images. During the navigation, the control law is derived from the difference between the visual features such as points and lines which are extracted from the current image and correlated stored image [7,8]. The nongeometric feature such as mutual information also can be used for navigation [9]. Besides the visual navigation, another widely attentional research is visual stabilization for the mobile robot, which is more difficult than tracing control due to the Brockett's necessary condition [10]. The external visual sensor is effective to increase the robustness of the closed-loop mobile robot system to the environment. While it brings the system various uncertainties because of imprecise or even uncalibrated camera parameters and the lack of depth information. Intensive researches have been investigated to solve the uncalibrated visual servoing problem for robot manipulators through the image Jacobian matrix [11–13]. Unfortunately, these approaches cannot be directly implemented on nonholonomic mobile robots due to nonholonomic constraints.

For mobile robots, a common strategy used to study the geometric constraints between images is adopted to realize the visual stabilization with uncalibrated intrinsic camera parameters. The epipolar geometry defined by the current and desired images, which is isomorphic to the planar geometric setup between the initial

pose and desired one of the robot system, is exploited to develop the system kinematics [14–16]. The three-dimensional distance is unknown as well as the intrinsic camera parameters. However, the epipolar geometry model is problematical with short baseline and is ill-conditioned for planar scenes. To deal with this issue, a planar projection homography-based methods are proposed in [17,18], in which the elements are organized to rebuild the system model. The chosen elements represent the relationship about the current pose of the robot system associated with the desired one. By doing so, a multi-step strategy is applied to control the translational error and angular error, respectively. Similar work is provided in [19], where the translational and angular errors could be simultaneously regulated to zero. A unified control law for visual stabilization and visual tracking is designed in [20]. Since trifocal tensor contains all the geometric relationships among the three views, which makes it independent of the observed scene. It is applied in [21,22] to overcome the drawbacks of the epipolar geometry and homography-based methods. In the aforementioned geometric constraint-based control methods, the intrinsic camera parameters are not needed to be calibrated. Unfortunately, extrinsic camera parameters are not considered. It is often assumed that the mobile robot can perform pure rotations on the spot, with the camera centered on the rotation axis, which does not correspond with the general case.

Few studies have yielded the visual stabilization of mobile robots with extrinsic camera parameters. In [23,24], an interaction matrix is used to describe the visual servoing system with the well-calibrated extrinsic camera parameters. Another homography-based method proposed in [25] considers two uncertain translational extrinsic camera parameters. The homography matrix is decomposed to obtain the three-dimensional information which is utilized to develop a rotational and translational error system between the current pose and the fixed reference pose. Adaptive updating laws using Lyapunov-based techniques are generated to compensate for the uncertain extrinsic camera parameters and unknown depth. In [26,27], an uncertain rotational extrinsic camera parameter is added which could be identified beforehand. It helps to convert the visual system into a simpler form as that in [25]. However, homography calculation and decomposition require a precise calibration of the intrinsic camera parameters. The adaptive laws can only compensate for the system uncertainties arising from uncertain translational extrinsic camera parameters and a constant depth parameter but not the calibration error of the intrinsic camera parameters.

Therefore, it is really a big issue on how to realize visual stabilization of nonholonomic mobile robots

with both uncalibrated intrinsic and extrinsic camera parameters. For controlling the mobile robot with nonholonomic constraints, most existing works can mainly be categorized into discontinuous time-invariant control method [28], time-varying control method [29] and hybrid of the former two methods [30]. However, the uncertainties arising from the vision system are not considered. In the conventional control theory, an observer could be constructed to estimate the system uncertainties. The extended state observer (ESO) is such a powerful scheme to deal with the nonlinear systems with mixed uncertain dynamics and disturbances. It is the key link toward the active disturbance rejection control (ADRC) framework which was initially put forward by Han [31]. The ADRC with dual-loop structure has outstanding strengths to deal with the uncertainties and nonholonomic constraints of the mobile robot separately. The total disturbance lumping the vast kinds of internal uncertainties and unknown external disturbance together is formulated as an extended state [32]. Then an ESO is reconstructed by the input–output data to estimate the total disturbance. Furthermore, the rigorous theoretical analyses of the ADRC including ESO for nonlinear uncertain systems are given in [33–35], which provide a theoretical foundation to flexibly use it in settling challenging problems.

In this study, a new image-based visual servoing scheme is proposed to stabilize the nonholonomic mobile robot equipped with a monocular camera. Firstly, system states are defined in the image plane by a coordinate transformation of the feature points. Thus, the kinematic system model with equal input and output dimensions is developed. To realize the uncalibrated visual servoing for the nonholonomic mobile robot, a dual-loop control structure is presented. By this strategy, the nonholonomic constraints and system uncertainties can be separately processed. In the inner loop, a linear ESO with reduced order is designed to estimate the system uncertainties caused by the uncalibrated camera parameters and unknown depth as well as the external disturbance. Then a nonlinear switching controller is established in the outer loop to make the system errors piecewise asymptotically converge. A subgoal on the image plane is utilized to produce a backward manoeuvre of the mobile robot. Finally, simulations and real-world experiments are given to validate the proposed scheme.

The remainder of the paper is organized as follows. Section 2 defines the coordinate relationship and describes the system model of the monocular mobile robot system, where the coordinate system is defined in the image plane. Section 3 presents the dual-loop control structure. An image-based visual servoing controller is designed based on a nominal model which

is compensated for by the linear ESO designed in the inner loop. Sections 4 and 5 show the performance of the proposed strategy via simulations and experiments, respectively. The last section gives the conclusions.

2. System modeling

In this section, the kinematics of the mobile robot with a monocular camera is developed in two steps. The degree of freedom of the control input is less than that of the system output in nonholonomic systems. After introducing the vision feedback, a new visual feature vector is defined to reconstruct the system model, leading to equal input and output dimensions.

2.1. Robot kinematics

The mobile robot with a fixed on-board camera and the coordinate relationships are described in Figure 1. Let $\mathcal{F}_r, \mathcal{F}_c$ denote the robot and camera frame, and $\mathcal{F}_r^*, \mathcal{F}_c^*$ denote the desired configuration of the robot and camera frame, respectively. All the frames are defined in right-handed form. The translational extrinsic camera parameters $a, b \in \mathbb{R}$ between the robot frame and camera frame are in axis x, z , respectively. The rotational extrinsic parameter $\phi \in \mathbb{R}$ is a deflection angle around the y axis. The three-dimensional coordinates of the feature points in the camera frames $\mathcal{F}_c, \mathcal{F}_c^*$ are defined as $\mathbf{P}_i^c = [X_i^c, Y_i^c, Z_i^c]^T \in \mathbb{R}^3$ and $\mathbf{P}_i^* = [X_i^*, Y_i^*, Z_i^*]^T \in \mathbb{R}^3$, respectively. The posture state vector of the mobile robot is described as $(x(t), z(t), \theta(t))^T \in \mathbb{R}^3$, where $(x(t), z(t))$ is the position coordinate of the mobile robot in the Cartesian space, and $\theta(t)$ is the rotational angle between \mathcal{F}_r and \mathcal{F}_r^* . The kinematics of the mobile robot can be

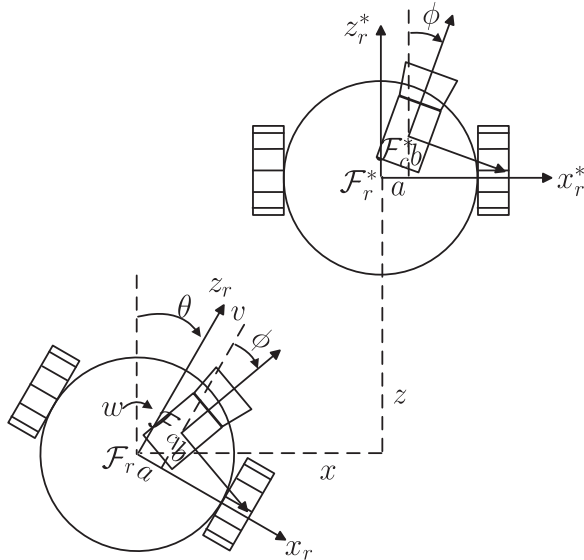


Figure 1. Coordinate relationships of the robot system.

expressed as

$$\begin{bmatrix} \dot{x} \\ \dot{z} \\ \dot{\theta} \end{bmatrix} = \begin{bmatrix} \sin \theta & 0 \\ \cos \theta & 0 \\ 0 & 1 \end{bmatrix} \underbrace{\begin{bmatrix} v_r \\ w_r \end{bmatrix}}_{U_r}, \quad (1)$$

where v_r and w_r denote the linear and angular velocities, respectively, being the control inputs of the mobile robot.

Then the mobile robot input $(v_r, w_r)^T$ is associated with the velocity twist $(v_{cx}, v_{cz}, w_c)^T$ of the camera by using the robot Jacobian matrix \mathbf{J}_r , expressed in the moving camera frame \mathcal{F}_c as follows:

$$\begin{bmatrix} v_{cx} \\ v_{cz} \\ w_c \end{bmatrix} = \underbrace{\begin{bmatrix} -\sin \phi & a \sin \phi + b \cos \phi \\ \cos \phi & b \sin \phi - a \cos \phi \\ 0 & 1 \end{bmatrix}}_{\mathbf{J}_r} \begin{bmatrix} v_r \\ w_r \end{bmatrix}. \quad (2)$$

Remark 2.1: One rotational and two translational extrinsic camera parameters are considered because they are sufficient to represent the camera configuration in many applications. This camera configuration is also used in some related works [23,26,27].

2.2. Coordinate transformation

As shown in Figure 2, two new features are defined in the image plane by the coordinate transformation of two image points. Let $\mathbf{p}_d = [u_{1d}, v_{1d}, u_{2d}, v_{2d}]^T \in \mathbb{R}^4$ be the goal feature vector which is taken at the desired configuration. It should be pointed out that the goal feature points are chosen to satisfy $v_{1d} = v_{2d}$. And $\mathbf{p}_c = [u_1, v_1, u_2, v_2]^T \in \mathbb{R}^4$ is the current feature vector. Then define a family of circle

$$\mathcal{P} = \{(u, v) : (u - u_0 - r)^2 + (v - v_0)^2 = r^2\} \quad (3)$$

in the image space, where (u_0, v_0) is the midpoint of the goal feature points. Then the midpoint (u_0, v_0) and the

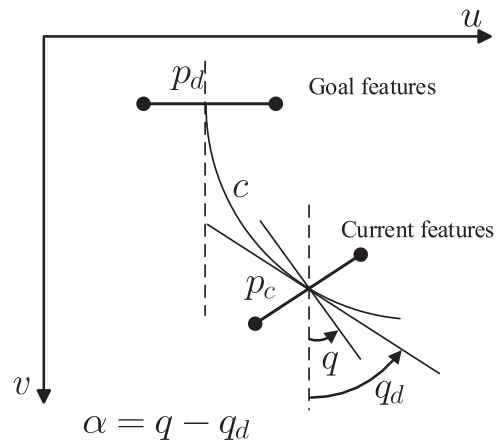


Figure 2. Coordinate transformation in image plane.

midpoint (u_c, v_c) of the current feature points are connected by these circles. The goal features satisfy $v_{1d} = v_{2d}$, which guarantees the circles centering on the line $v = v_0$ with $\frac{\partial u}{\partial v} = 0$ at $v = v_0$. The arc length between (u_0, v_0) and (u_c, v_c) is defined as the image radian error c . The tangent angle of \mathcal{P} at (u_c, v_c) is denoted by q_d , and the image orientation error calculated by the current image points \mathbf{p}_c is denoted by q . There are

$$\begin{aligned} q &= \arctan \frac{v_2 - v_1}{u_2 - u_1}, \\ q_d &= 2 \arctan \frac{u_c - u_0}{v_0 - v_c}, \\ c &= r q_d = \frac{1}{2} \frac{(u_c - u_0)^2 + (v_c - v_0)^2}{u_c - u_0} q_d. \end{aligned} \quad (4)$$

Then a new system state vector is defined as

$$\mathbf{f} = \begin{bmatrix} c \\ \alpha \end{bmatrix} \in \mathbb{R}^2, \quad (5)$$

where $\alpha = q - q_d$. Note that \mathbf{f} is a smooth function of \mathbf{p}_c , which means it is differentiable with respect to \mathbf{p}_c .

2.3. System kinematics

Without loss of generality, a camera-robot system can be developed by differentiating (5) with respect to time as follows:

$$\dot{\mathbf{f}} = \frac{d}{dt} \begin{bmatrix} c \\ \alpha \end{bmatrix} = \frac{\partial \mathbf{f}}{\partial \mathbf{p}_c} \mathbf{J}_c \mathbf{J}_r \mathbf{U}_r = \mathbf{J}_i \mathbf{J}_c \mathbf{J}_r \mathbf{U}_r, \quad (6)$$

where

$$\begin{aligned} \mathbf{J}_i &= \begin{bmatrix} l_1 & l_2 & l_1 & l_2 \\ l_3 + l_5 & l_6 - l_4 & l_5 - l_3 & l_4 + l_6 \end{bmatrix}, \\ l_1 &= \frac{1}{2} \left(\frac{(u_c - u_0)^2 - (v_c - v_0)^2}{2(u_c - u_0)^2} q_d - \frac{v_c - v_0}{u_c - u_0} \right), \\ l_2 &= \frac{1}{2} \left(1 - \frac{v_0 - v_c}{u_c - u_0} q_d \right), \\ l_3 &= \frac{v_2 - v_1}{(u_2 - u_1)^2 + (v_2 - v_1)^2}, \\ l_4 &= \frac{u_2 - u_1}{(u_2 - u_1)^2 + (v_2 - v_1)^2}, \\ l_5 &= \frac{v_c - v_0}{(u_c - u_0)^2 + (v_c - v_0)^2}, \\ l_6 &= -\frac{u_c - u_0}{(u_c - u_0)^2 + (v_c - v_0)^2}, \end{aligned} \quad (7)$$

and $\mathbf{J}_c \in \mathbb{R}^{4 \times 3}$ is the image Jacobian or interaction matrix defined in [36]. \mathbf{J}_r is defined in (2). Due to the mobile

robot moving on a plane, the motion along y -axis does not happen so that the height of the feature points maintains constant during the visual servoing task. The relationship can be represented as

$$Y_i^c = Y_i^*, \quad i = 1, 2, \quad (8)$$

and \mathbf{J}_c can be formulated as

$$\mathbf{J}_c = \begin{bmatrix} -\frac{f_u}{Z_1^c} & \frac{u_1}{Z_1^c} & -f_u - \frac{u_1^2}{f_u} \\ 0 & \frac{v_1}{Z_1^c} & -\frac{u_1 v_1}{f_u} \\ -\frac{f_u}{Z_2^c} & \frac{u_2}{Z_2^c} & -f_u - \frac{u_2^2}{f_u} \\ 0 & \frac{v_2}{Z_2^c} & -\frac{u_2 v_2}{f_u} \end{bmatrix}. \quad (9)$$

According to the geometric relation of the perspective projection of the pinhole camera model, the variables $\frac{1}{Z_i^c}$ is calculated as

$$\frac{1}{Z_i^c} = \frac{v_i}{f_v Y_i^c}, \quad i = 1, 2, \quad (10)$$

where f_u, f_v are the unknown camera focal lengths in pixel dimensions. Then substituting (2), (7), (8), (9), (10) to (6), the system kinematic model could be obtained

$$\dot{\mathbf{f}} = \underbrace{\begin{bmatrix} \sum_{i=3}^6 G_{i+4} F_i & \sum_{i=1}^6 G_i F_i \\ \sum_{i=3}^6 G_{i+4} F_{i+6} & \sum_{i=1}^6 G_i F_{i+6} \end{bmatrix}}_{\mathbf{H}(\mathbf{p}_c)} \mathbf{U}_r, \quad (11)$$

where $\mathbf{H}(\mathbf{p}_c) \in \mathbb{R}^{2 \times 2}$ is the system matrix containing all unknown constants with respect to the camera parameters and three-dimensional scene information. The details are given in the Appendix.

3. Control strategy design and analysis

The vision-based set-point stabilization task is to converge the image radian error c and the state α to zero simultaneously. Meanwhile, the visual features should keep in the field of view during the stabilization task of the nonholonomic mobile robot. However, since these two states are defined as relative values with respect to the goal position, the system matrix $\mathbf{H}(\mathbf{p}_c)$ will be singular at the goal position which is analyzed in [37]. Thus, a switching strategy is adopted to ensure the new system states converge around the goal position. In addition, the inverse of the system matrix $\mathbf{H}(\mathbf{p}_c)$ cannot be directly calculated due to the unknown constant vector \mathbf{G} . In order to realize the visual servoing task, the control scheme

should be established to deal with the unmodeled uncertainty in $\mathbf{H}(\mathbf{p}_c)$ and external disturbance. The ADRC provides a frame that considers the control performance and robustness of the nonlinear system (11) separately, in which ESO is the key part to estimate the uncertainties on-line.

From the above analysis, a dual-loop structure of the proposed strategy for the mobile robot visual servoing system is shown in Figure 3. A linear ESO is designed to estimate the uncertainties and compensate to the controller. Rewrite the system model (11) to a suitable form with the total disturbance as follows:

$$\dot{\mathbf{f}} = \underbrace{\begin{bmatrix} \sum_{i=3}^6 \hat{G}_{i+4} F_i & \sum_{i=1}^6 \hat{G}_i F_i \\ \sum_{i=3}^6 \hat{G}_{i+4} F_{i+6} & \sum_{i=1}^6 \hat{G}_i F_{i+6} \end{bmatrix}}_{\hat{\mathbf{H}}(t)} \mathbf{U}_r + \mathbf{D}(t), \quad (12)$$

where $\hat{\mathbf{G}}$ is a roughly estimated parameter vector, and $\hat{\mathbf{H}}(t)$ is a function of the image points \mathbf{p}_c . $\mathbf{D}(t)$ denotes the total disturbance including the system uncertainty and external disturbance defined as

$$\mathbf{D}(t) = (\mathbf{H}(\mathbf{p}_c) - \hat{\mathbf{H}}(t)) \mathbf{U}_r + d(t), \quad (13)$$

where $d(t)$ is the external disturbance which is bounded and its change rate with respect to time t is also bounded such that $\|d(t)\| \leq \bar{d}$, $\|\dot{d}(t)\| \leq \bar{\dot{d}}$. Then suppose the total disturbance $\mathbf{D}(t)$ to satisfy the following inequality for positive constants γ_1 and γ_2

$$\|\mathbf{D}(t)\| \leq \gamma_1 + \gamma_2 \|f\|. \quad (14)$$

A normal linear ESO is constructed for (12) to estimate the $\mathbf{D}(t)$ in real-time

$$\begin{aligned} \dot{\mathbf{Z}}_1 &= \mathbf{Z}_2 + \hat{\mathbf{H}}(t) \mathbf{U}_r - \beta_1 (\mathbf{Z}_1 - \mathbf{f}), \\ \dot{\mathbf{Z}}_2 &= -\beta_2 (\mathbf{Z}_1 - \mathbf{f}), \end{aligned} \quad (15)$$

where the positive parameters β_1, β_2 should be tuned such that the output \mathbf{Z}_2 of ESO can estimate the total disturbance $\mathbf{D}(t)$. Since the output of the system \mathbf{f} does not need to be estimated, the following reduced order ESO

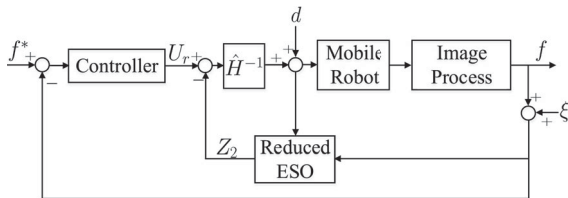


Figure 3. Framework of the ESO-based control strategy.

[33] is designed

$$\begin{aligned} \dot{\mathbf{Z}} &= -\beta \mathbf{Z} - \beta^2 \mathbf{f} - \beta \hat{\mathbf{H}}(t) \mathbf{U}_r, \\ \mathbf{Z}_2 &= \mathbf{Z} + \beta \mathbf{f}, \quad \beta > 0 \end{aligned} \quad (16)$$

Since the initial condition of (15) is always selected as

$$\mathbf{Z}_i(t_0) = \mathbf{0}, \quad i = 1, 2,$$

we have

$$\mathbf{Z}(t_0) = -\beta \mathbf{f}(t_0).$$

Using the Laplace operator s on (16), there is

$$s\mathbf{Z}_2 = -\beta \mathbf{Z} - \beta^2 \mathbf{f} - \beta \hat{\mathbf{H}} \mathbf{U}_r + \beta s \mathbf{f}. \quad (17)$$

Then substitute $\mathbf{D} = s\mathbf{f} - \hat{\mathbf{H}} \mathbf{U}_r$ to (17), lead to

$$\mathbf{Z}_2 = \frac{\beta}{s + \beta} \mathbf{D}. \quad (18)$$

The parameter β is regarded as the bandwidth of the reduced-order ESO (16), which is instead of β_1, β_2 to be tuned. By using the estimation \mathbf{Z}_2 , a nonlinear feedback controller can be designed as

$$\begin{aligned} \mathbf{U}_r &= \hat{\mathbf{H}}^{-1}(t) (-\mathbf{K} \mathbf{U}_0 - \mathbf{Z}_2), \\ \mathbf{U}_0 &= \text{diag} \{ \text{fal}(c, \epsilon, \delta), \text{fal}(\alpha, \epsilon, \delta) \}. \end{aligned} \quad (19)$$

The nonlinear function $\text{fal}(e, \epsilon, \delta)$ defined in [32] has satisfactory performance that large error gives small output as well as small error gives large output which can balance the difference between two states of different orders of magnitude.

This control law will enable the system converge to the equilibrium point asymptotically. However, the matrix $\hat{\mathbf{H}}$ is singular at the goal position. That is to say the gain of the controller (19) declines rapidly when the image radian error c is close to zero. Unfortunately, this will happen with a nonzero image orientation error, i.e. $q \neq 0$. What we expect is that the image orientation error converges faster than the image radian error. The overall control procedures with a switchback strategy is described in several steps:

- (1) Pre-record an image at the desired posture as the reference and extract the goal image points. Then calculate the corresponding midpoint and new state variables.
- (2) Enter the control loop and track the image features.
- (3) If the midpoint (u_c, v_c) is close to the goal midpoint (u_0, v_0) with a nonzero image orientation error, a subgoal will be regarded as the new reference in next iteration of the control loop. The switching conditions are $|u_c - u_0| \leq \bar{u} \in \mathbb{Z}$, $|v_c - v_0| \leq \bar{v} \in \mathbb{Z}$ with

the image orientation error $|q| \geq \bar{q} \in \mathbb{R}$, where \bar{u} , \bar{v} , \bar{q} are given thresholds.

- (4) The switched subgoal will be judged in the same way. If the midpoint (u_c, v_c) is close to the subgoal with a nonzero image orientation error, then reset the reference point to the goal midpoint (u_0, v_0) .
- (5) The control law is computed by (19) during the whole task.
- (6) Make sure the switching happens in pairs before the system states converge around the goal position.

The subgoal reference point is chosen as $(u'_0, v'_0) = (-k_1 \hat{G}_1 q, k_2 v_0)$, where $k_1 \in \mathbb{R}, 0 < k_2 < 1$. A heuristic method is used to choose the subgoal. The purpose is to drive the mobile robot retreat and simultaneously reduce the lateral error. Since Y_i^c does not change during the task, the ordinate of the image point is determined by Z_i^c which denotes the distance from the camera to the feature point along z -axis. Thus, we choose a subgoal whose ordinate is smaller than the ordinate of the goal such that $v'_0 < v_0$, which will realize the retreat of the mobile robot. In order to reduce the lateral error along x -axis, the abscissa of the subgoal is empirically chosen according to that in [37].

According to above design procedure of the control strategy, a unified controller is designed. Actually, the set-point stabilization problem of the mobile robot is changed into a tracking control problem of an aperiodic square wave reference. The reference signal is regarded as

$$f_d(t) = \begin{cases} 0, & t_{2i} \leq t < t_{2i+1}, \\ f_{di}, & t_{2i+1} \leq t < t_{2i+2}, \end{cases} \quad i = 0, 1, \dots, n, \quad (20)$$

and $\lim_{t \rightarrow \infty} f_d(t) = 0$. A Lyapunov function is defined as $V_1 = \frac{1}{2} \mathbf{e}^T \mathbf{e}$ with $\mathbf{e} = \mathbf{f} - \mathbf{f}_d$, the derivative of V_1 is given as

$$\dot{V}_1 \leq -\|\mathbf{K}\mathbf{e}\| \text{fal}(\|\mathbf{e}\|, \epsilon, \delta) + \|\mathbf{e}\| \|\boldsymbol{\xi}\|, \quad (21)$$

where $\boldsymbol{\xi} = \mathbf{D} - \mathbf{Z}_2$. From (18), we get $\boldsymbol{\xi} = s/(s + \beta)\mathbf{D}$, the state space realization of linear ESO can be developed as

$$\begin{aligned} \dot{\mathbf{x}} &= -\beta \mathbf{x} - \beta \mathbf{D}, \\ \boldsymbol{\xi} &= \mathbf{x} + \mathbf{D}. \end{aligned} \quad (22)$$

Then a new Lyapunov function for the whole closed-loop system is defined as $V = V_1 + \frac{1}{2} \mathbf{x}^T \mathbf{x}$. Based on (14), the derivative of V is deduced as

$$\begin{aligned} \dot{V} &\leq -\left(\|\mathbf{K}\| \frac{\text{fal}(\|\mathbf{e}\|, \epsilon, \delta)}{\|\mathbf{e}\|} - \gamma_2 - \frac{\gamma_1}{\mu_1} - \frac{1 + \beta\gamma_2}{\mu_2}\right) \|\mathbf{e}\|^2 \\ &\quad - \left(\beta - \frac{\beta\gamma_1}{\mu_3} - \frac{1 + \beta\gamma_2}{\mu_2}\right) \|\mathbf{x}\|^2 \\ &\quad + \gamma_2 (\|\mathbf{e}\| + \beta \|\mathbf{x}\|) \|\mathbf{f}_d\|, \end{aligned} \quad (23)$$

where μ_1, μ_2 and μ_3 are positive constants. Since $\lim_{t \rightarrow \infty} f_d(t) = 0$, \dot{V} will be strictly negative via choosing appropriate controller parameters \mathbf{K} and ESO bandwidth β . Thus, it can be inferred that the system states can converge to a compact set and the closed-loop system is asymptotically stable.

4. Simulations

In this section, simulations are introduced to validate the proposed control strategy. The virtual camera parameters are set as $f_u = 931.18$, $f_v = 896.5$, $a = 0$, $b = 0.1$, $\phi = 10^\circ$. $P_1 = [1.3, -0.1, 0.745]m$, $P_2 = [1.2, -0.3, 0.735]m$ are the selected feature points which have the same image ordinates at the desired configuration $(x^*, z^*, \theta^*) = (0m, 0m, 0^\circ)$. A random Gaussian noise with a deviation of 0.5 pixels, is added into the image points to verify the robustness of the strategy. A reasonable guess of the estimated constant vector $\hat{\mathbf{G}}$ is taken as

$$\hat{\mathbf{G}} = [950, 1.05 \times 10^{-3}, 0.4224, 0.4224, 9.4505 \times 10^{-5}, 9.4505 \times 10^{-5}, 0.8978, 0.8978, 0.0044, 0.0044]^T$$

to observe the control performance. This guess could be the possible value in a limited region around the true value. Then the control parameters and thresholds are selected as $\beta = 3$, $\mathbf{K} = \text{diag}\{0.075, 0.5\}$, $\epsilon_1 = 0.25$, $\delta_1 = 1$, $\epsilon_2 = 0.1$, $\delta_2 = 1$, $k_1 = -6.5$, $k_2 = 0.6$ and $\bar{u} = 10$ pixel, $\bar{v} = 10$ pixel, $\bar{q} = 0.01$. Due to the pose of switching to subgoal is around the desired posture, a sudden increase in the image error will generate a large control law which is easy to lose the image points. Thus, the control gain matrix is tuned to a smaller value $\mathbf{K} = \text{diag}\{0.05, 0.35\}$ when the subgoal is viewed as the reference point to avoid the feature points out of the field of view. Two different initial postures with a small lateral deviation and a large lateral deviation are illustrated, which is set at $(x, z, \theta) = (-1.6928m, -0.3m, 21^\circ)$ and $(-1.6928m, -0.5571m, 21^\circ)$, respectively.

The trajectories followed by the two image points of the two different initial poses, starting from the circular points and ending at the star points are displayed in Figures 4 and 6, respectively. As expected, the feature points approximately move toward the goal features along an arc which pass through the midpoints of the goal features and current features. Therefore, the image trajectories always concentrate around the arc, which considerably decreases the possibility of missing features during the task. The motion path of the initial pose with a small lateral deviation is a smooth trajectory observed in Figure 5, where the bold triangle at the origin denotes the desired pose. The triangular trajectory is drawn with a sampling interval set as 20. No switching is needed in

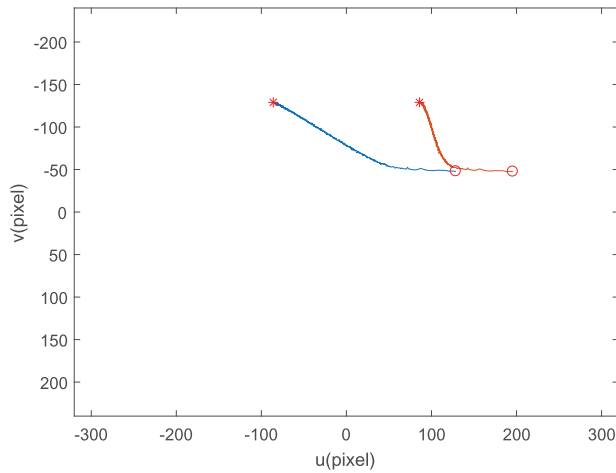


Figure 4. Simulation of the initial posture (-1.6928 m, -0.3 m, 21°): feature trajectories.

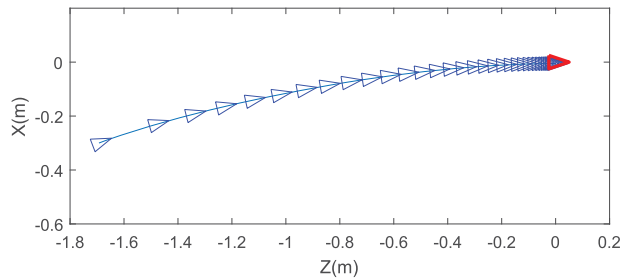


Figure 5. Simulation of the initial posture (-1.6928 m, -0.3 m, 21°): motion path of stabilization.

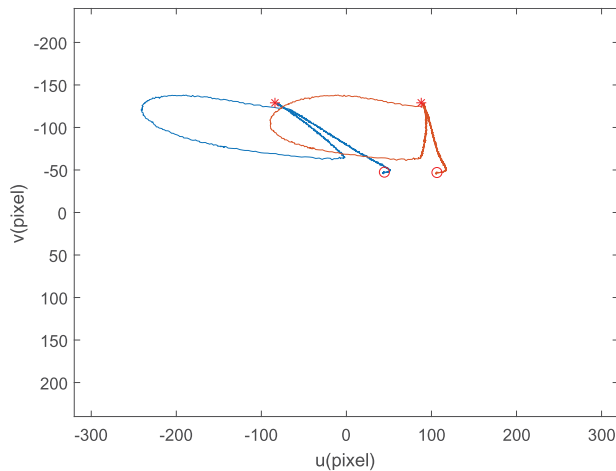


Figure 6. Simulation of the initial posture (-1.6928 m, -0.5571 m, 21°): feature trajectories.

the small lateral deviation case and the states converge to zero asymptotically. The motion path with a large lateral deviation is shown in Figure 7. It takes one switchback for the mobile robot to arrive at its desired pose with enough small steady-state errors.

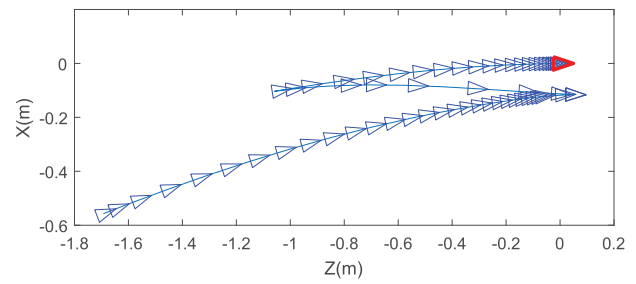


Figure 7. Simulation of the initial posture (-1.6928 m, -0.5571 m, 21°): motion path of stabilization.

5. Experiments

5.1. Experimental setup

The control strategy is verified on a mobile robot testbed as depicted left in Figure 8. The robot is composed by a two-wheel differential platform that the wheel encoder information is not open to users, an inclusive Conroe 2.9-GHz processor mini-PC manufactured by Intel, and a CCD camera that captures 30 frames in one second with a size of 640×480 pixels. The experiments are performed in the ROS (robot operating system) [38]. In order to predigest the subsequent image processing so that the readers can focus on the main result, we design a field layout where it is easy to get two image points with the same ordinates at an unrestricted desired configuration. As shown right in Figure 8, two reference markers are attached at a similar height on an object and extracted by directly using the feature detectors of the OpenCV library. The center of the circles will be extracted as the feature points and utilized to the control scheme. The total time of a control period and image processing time is within 30 ms. The frequency that mini-PC sends control inputs to the mobile platform through an RS232 serial port is set at 30 Hz.

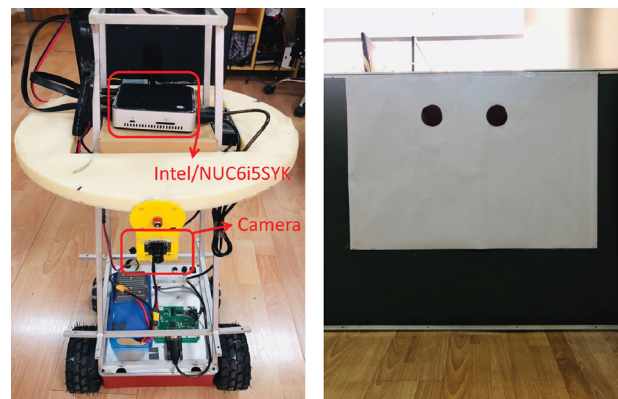


Figure 8. Mobile robot testbed (left) and target object with two markers (right).

5.2. Control constraints

In view of the physical constraints on the actuators of the mobile robot and the velocity mutation during switching, even more conservative bounds on velocities are considered as

$$|v| \leq v_{\max} = 0.2 \text{ m/s}, \quad |w| \leq w_{\max} = 0.3 \text{ rad/s}.$$

Then a velocity scaling defined in [39]

$$\sigma = \max\{|v|/v_{\max}, |w|/w_{\max}, 1\}$$

is performed. And the actual commands v_r and w_r are calculated as

$$\begin{aligned} v_r &= \text{sign}(v) v_{\max}, w_r = w/\sigma, & \text{if } \sigma &= |v|/v_{\max}, \\ v_r &= v/\sigma, w_r = \text{sign}(w) w_{\max}, & \text{if } \sigma &= |w|/w_{\max}, \\ v_r &= v, w_r = w, & \text{if } \sigma &= 1. \end{aligned}$$

5.3. Results

In this subsection, the control performance and robustness of the strategy is verified via two groups of experiments. The control parameters and thresholds are selected as $\beta = 3$, $K = \text{diag}\{0.02, 0.1\}$, $\epsilon_1 = 0.25$, $\delta_1 = 1$, $\epsilon_2 = 0.1$, $\delta_2 = 1$, $k_1 = 2$, $k_2 = 0.7$ and $\bar{u} = 10$ pixel, $\bar{v} = 10$ pixel, $\bar{q} = 0.01$. The control gain matrix is tuned to a smaller value $K = \text{diag}\{0.002, 0.04\}$ when the subgoal is regarded as the reference point.

In the first experiment, the extrinsic camera parameters are roughly measured with a tapeline as $a \approx 0$ m, $b \approx 0.10$ m, the estimation of the rotational extrinsic parameter is set as $\phi = 0$, the camera focal length is estimated as $f_u \approx 950$ pixel and the unknown constants are estimated as $c_1 = c_2 \approx 180$. Thus, the vector \hat{G} can be calculated as

$$\hat{G} = [950, 1.05 \times 10^{-3}, -0.556, -0.556, 0, 0, 0, 0, 5.848 \times 10^{-3}, 5.848 \times 10^{-3}]^T.$$

Two initial postures are randomly selected by manually controlling the mobile robot move to $(-1.556 \text{ m}, -0.188 \text{ m}, 8.53^\circ)$ and $(-1.756 \text{ m}, -0.375 \text{ m}, 21.37^\circ)$ through a keyboard. The results of the first posture with a small lateral deviation are shown in Figures 9–12. The feature trajectories are shown in Figure 9 are similar to the arcs and the motion path of the stabilization task of the mobile robot displayed in Figure 10 is smooth. The experimental results validate the switching is not needed for an initial pose with small lateral deviation. The evolution of the robot posture vector is depicted in Figure 11, where the dashed line denotes the desired value. The final posture is located at $(-0.0046 \text{ m}, -0.0081 \text{ m}, 0.0573^\circ)$. The postural information is recorded from the odom (the

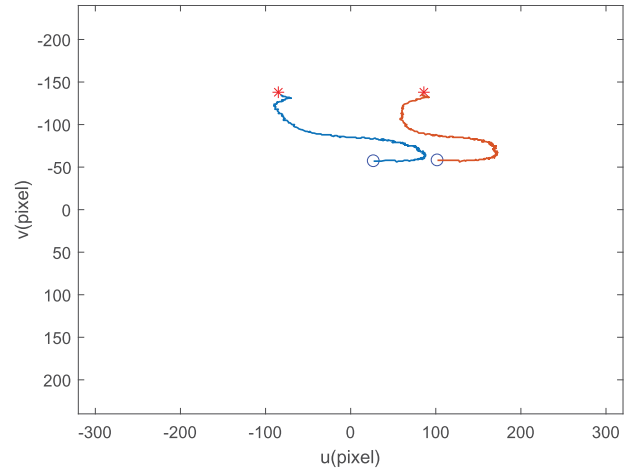


Figure 9. Experimental results of the initial posture $(-1.556 \text{ m}, -0.188 \text{ m}, 8.53^\circ)$: feature trajectories.

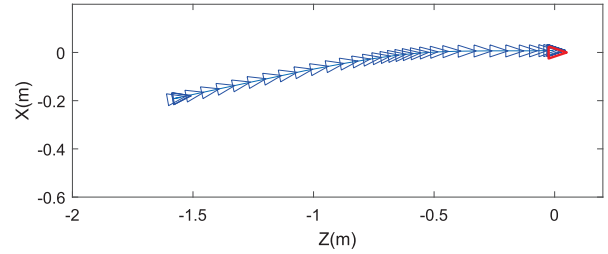


Figure 10. Experimental results of the initial posture $(-1.556 \text{ m}, -0.188 \text{ m}, 8.53^\circ)$: motion path of stabilization.

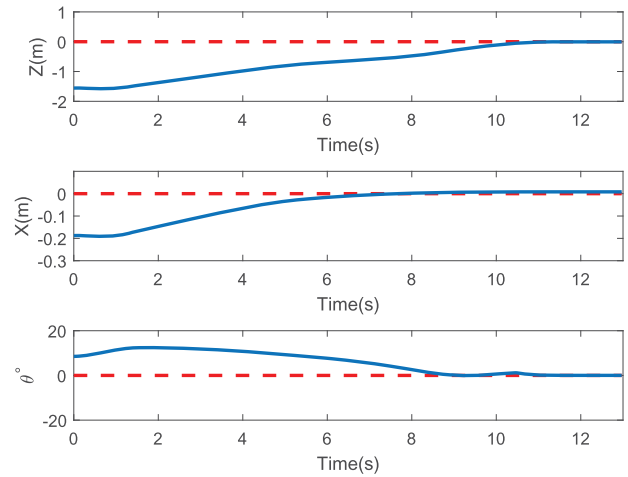


Figure 11. Experimental results of the initial posture $(-1.556 \text{ m}, -0.188 \text{ m}, 8.53^\circ)$: posture vector of the mobile robot.

topic in ROS) which is iteratively calculated by using the velocities, recorded in Figure 12.

During the experiment of the second initial pose, the images captured at five different poses are displayed in Figure 13. Two stationary annuluses represent the desired

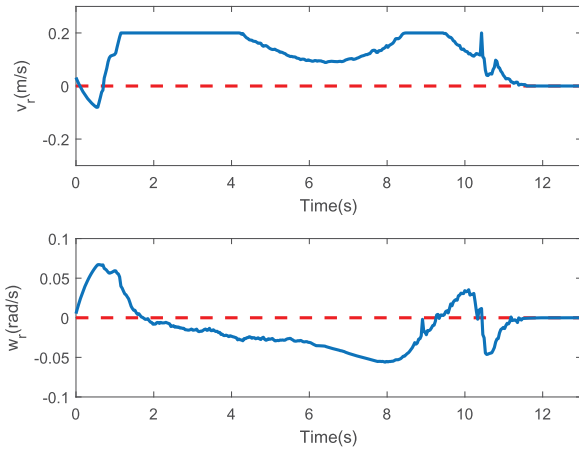


Figure 12. Experimental results of the initial posture (-1.556 m, -0.188 m, 8.53°): control inputs.

positions of the features, and the smaller one is the subgoal which is computed in real time. The dots represent the current feature positions and the midpoint, respectively. Figure 14 shows the feature trajectories. The motion path and state vector are displayed in Figures 15 and 16. It also takes one switchback for the mobile robot to arrive at its desired pose. The final posture is located at (-0.0084 m, -0.0109 m, -0.5959°). The symbols ‘ \times ’ on the curves shown in Figures 16 and 17 denote the switching time. The velocities of the mobile robot are depicted in Figure 17. Although the saturated inputs are executed in the experiment, the similar control performance is obtained as that in the simulations.

The second experiment is conducted to demonstrate the robustness of the proposed control system

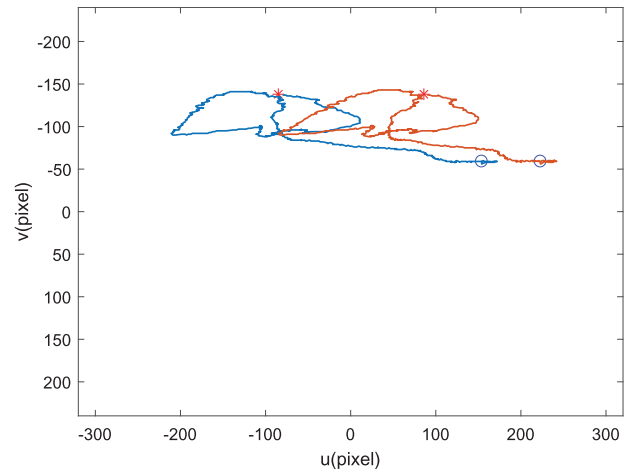


Figure 14. Experimental results of the initial posture (-1.756 m, -0.375 m, 21.37°): feature trajectories.

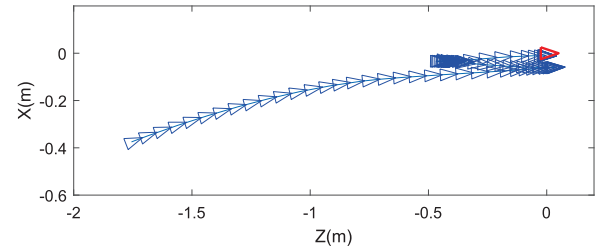


Figure 15. Experimental results of the initial posture (-1.756 m, -0.375 m, 21.37°): motion path of stabilization.

with the model uncertainties caused by the uncalibrated camera parameters. According to physical constants of the mobile robot testbed, the unknown parameters are made to vary in the ranges, $a \in [-0.2, 0.2]$ m, $b \in$

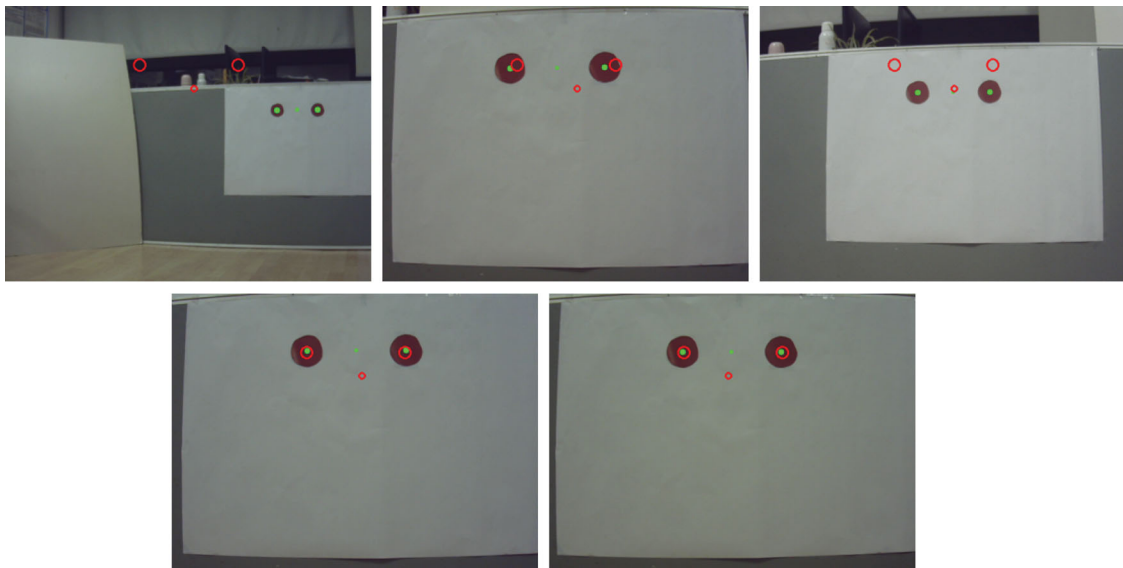


Figure 13. From top left to bottom right: the images captured at the initial posture, the posture of switching to subgoal, the posture of switching to goal, the final posture and the desired posture.

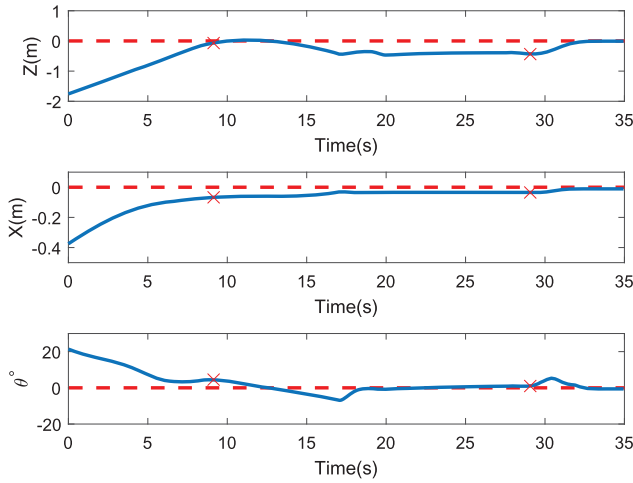


Figure 16. Experimental results of the initial posture ($-1.756 \text{ m}, -0.375 \text{ m}, 21.37^\circ$): posture vector of the mobile robot.

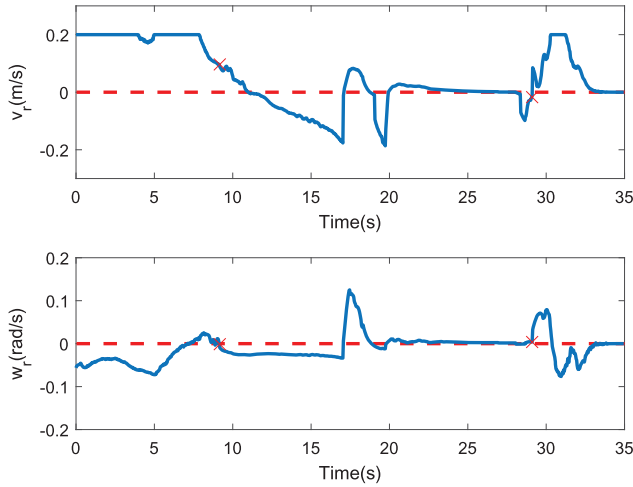


Figure 17. Experimental results of the initial posture ($-1.756 \text{ m}, -0.375 \text{ m}, 21.37^\circ$): control inputs.

$[-0.1, 0.1] \text{ m}, f_u \in [900, 1000] \text{ pixel}$. The performance of the proposed control strategy is evaluated through the following error measure over the control time,

$$E = \frac{1}{T} \int_0^T [e_x(t)^2 + e_z(t)^2 + e_\theta(t)^2] dt < \bar{E}, \quad (24)$$

where $e_x = x - x^*$, $e_z = z - z^*$, $e_\theta = \theta - \theta^*$ and \bar{E} is a defined threshold calculated by (24) with $a = 0 \text{ m}$, $b = 0.1 \text{ m}$, $f_u = 950 \text{ pixel}$. The initial pose is set at the same value ($-1.756 \text{ m}, -0.375 \text{ m}, 21.37^\circ$). All control parameters and switching thresholds are not retuned. Figure 18 depicts the regions of satisfactory performance for different camera parameters, where three values of f_u are chosen as examples. The designed controller has a wide range of variation of the unknown camera parameters, which means it is still effective when the camera moves

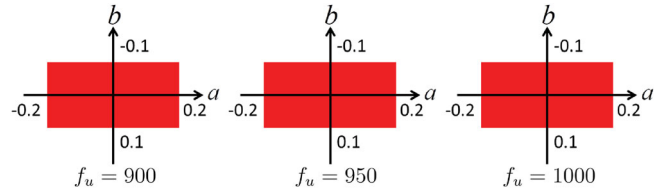


Figure 18. Regions of satisfactory performance for different values of the parameters a, b, f_u .

slightly on the robot or the focal length changes in different environment.

6. Conclusion

A new approach to the uncalibrated visual stabilization of nonholonomic mobile robots is provided. The uncalibrated camera parameters as well as the unknown depth bring internal uncertainties for the system. Then a linear reduced-order ESO is designed to estimate the system uncertainties. While in the outer loop, a coordinate transformation of the image points is implemented to reduce the number of system outputs to the number of inputs. Subsequently, the new state vector is defined to develop the system kinematics. The nonlinear feedback controller is designed for the nominal model, which is compensated for by the ESO. The simplicity of the controller design in the ADRC framework is kept for the visual servoing of the nonholonomic mobile robot. Meanwhile, the singularity of the system matrix at the goal position is solved by using a switchback strategy. Simulations and experiments demonstrate the proposed approach is effective and robust to the uncalibrated camera parameters.

ESO is first implemented to deal with the uncalibrated visual servoing for nonholonomic mobile robots. The rampart for its usage is that the degree of freedom of input and output of the conventional system model is not equal due to the nonholonomic constraints. This paper uses a radian error and an orientation error defined in the image plane as the new states to descend the dimension of the system output, which enables the ESO successfully applied. However, the system matrix will be singular at the goal position, which is unavoidable but not desirable. Although this problem could be solved by employing a switchback strategy, new states need to be found so that the ESO may behave better in the nonholonomic systems.

Disclosure statement

No potential conflict of interest was reported by the authors.

Funding

This work was partially financially supported by the National Natural Science Foundation of China (NSFC) [grant numbers 61533012 and 91748120].

Notes on contributors

Yao Huang received the BS degree from Tianjin Polytechnic University, Tianjin, and the MS degree in Instrument Science and Technology from the Shanghai University, Shanghai, China, in 2011 and 2014, respectively. She is currently working toward the PhD degree with the Department of Automation, Shanghai Jiao Tong University, Shanghai. Her research interests are in visual servoing and robotics.

Jianbo Su received the BS degree in Control Theory and Control Engineering from Shanghai Jiaotong University, Shanghai, China, in 1989, the MS degree in Pattern Recognition and Intelligent System from Institute of Automation, Chinese Academy of Sciences, Beijing, China, in 1992, and PhD in Control Theory and Control Engineering from Southeast University, Nanjing, China, in 1995. From 1995 to 1997, he was a postdoctoral research fellow in Robotics in Chinese Academy of Sciences. He is currently a professor in the Department of Automation, Shanghai Jiao Tong University. His research interests include robotics, pattern recognition and computer vision.

ORCID

Yao Huang  <http://orcid.org/0000-0001-6931-8963>

References

- [1] Tzafestas SG. Mobile robot control and navigation: a global overview. *J Intell Robot Syst.* **2018 Jul**;91(8):35–58.
- [2] Cadena C, Carlone L, Carrillo H, et al. Past, present, and future of simultaneous localization and mapping: toward the robust-perception age. *IEEE Trans Robot.* **2016**;32(6):1309–1332.
- [3] Lowry S, Suenderhauf N, Newman P, et al. Visual place recognition: a survey. *IEEE Trans Robot.* **2016 Feb**;32(1):1–19.
- [4] Gupta S, Tolani V, Davidson J, et al. Cognitive mapping and planning for visual navigation. *Int J Comput Vis.* **2019**;1–20.
- [5] Zhu Y, Mottaghi R, Kolve E, et al. Target-driven visual navigation in indoor scenes using deep reinforcement learning. 2017 IEEE International Conference on Robotics and Automation (ICRA); 2017 May 29–Jun 3; Singapore; 2017. p. 3357–3364.
- [6] Cristóforis PD, Nitsche M, Krajník T, et al. Hybrid vision-based navigation for mobile robots in mixed indoor/outdoor environments. *Pattern Recognit Lett.* **2015**;53:118–128.
- [7] Bista SR, Giordano PR, Chaumette F. Appearance-based indoor navigation by IBVS using line segments. *IEEE Robot Auton Lett.* **2016**;1(1):423–430.
- [8] Bista SR, Giordano PR, Chaumette F. Combining line segments and points for appearance-based indoor navigation by image-based visual servoing. 2017 IEEE/RSJ International Conference on Intelligent Robots and Systems (IROS); 2017 Sep 24–28; Vancouver, BC, Canada; 2017. p. 2960–2967.
- [9] Raj S, Giordano PR, Chaumette F. Appearance-based indoor navigation by IBVS using mutual information. 2016 14th International Conference on Control, Automation, Robotics and Vision (ICARCV); 2016 Nov 13–15; Phuket, Thailand; 2016. p. 1–6.
- [10] Brockett RW. Asymptotic stability and feedback stabilization. In: Brockett RW, Millman RS, Sussmann HJ, editors. *Differential geometric control theory*. 1983. p. 181–191.
- [11] Su J, Qiu W, Ma H, et al. Calibration-free robotic eye-hand coordination based on an auto disturbance-rejection controller. *IEEE Trans Robot.* **2004 Oct**;20(5):899–907.
- [12] Liu YH, Wang H, Wang C, et al. Uncalibrated visual servoing of robots using a depth-independent interaction matrix. *IEEE Trans Robot.* **2006**;22(4):804–817.
- [13] Ma Z, Su J. Robust uncalibrated visual servoing control based on disturbance observer. *ISA Trans.* **2015**;59:193–204.
- [14] Mariottini GL, Oriolo G, Prattichizzo D. Image-based visual servoing for nonholonomic mobile robots using epipolar geometry. *IEEE Trans Robot.* **2007**;23(1):87–100.
- [15] Lopez-Nicolas G, Sagues C, Guerrero JJ, et al. Switching visual control based on epipoles for mobile robots. *Robot Auton Syst.* **2008**;56(7):592–603.
- [16] Li B, Fang Y, Zhang X. Essential-matrix-based visual servoing of nonholonomic mobile robots without short baseline degeneration. *IEEE International Conference on Control Applications*; 2013 Aug 28–30; Hyderabad, India; 2013. p. 465–476.
- [17] Lopez-Nicolas G, Gans NR, Bhattacharya S, et al. Homography-based control scheme for mobile robots with nonholonomic and field-of-view constraints. *IEEE Trans Syst Man Cybern B (Cybern).* **2010 Aug**;40(4):1115–1127.
- [18] Li B, Fang Y, Zhang X. Visual servo regulation of wheeled mobile robots with an uncalibrated onboard camera. *IEEE/ASME Trans Mechatron.* **2016 Oct**;21(5):2330–2342.
- [19] Huang Y, Su J. Simultaneous regulation of position and orientation for nonholonomic mobile robot. 2016 International Conference on Machine Learning and Cybernetics (ICMLC). Vol. 2. 2016 Jul 10–13; Jeju, South Korea; 2016. p. 477–482.
- [20] Zhang K, Chen J, Li Y, et al. Unified visual servoing tracking and regulation of wheeled mobile robots with an uncalibrated camera. *IEEE/ASME Trans Mechatron.* **2018 Aug**;23(4):1728–1739.
- [21] Lopez-Nicolas G, Guerrero JJ, Sagues C. Visual control through the trifocal tensor for nonholonomic robots. *Robot Auton Syst.* **2010**;58(2):216–226.
- [22] Li B, Fang Y, Zhang X. 2d trifocal tensor based visual servo regulation of nonholonomic mobile robots. *Acta Autom Sinica.* **2014**;40(12):5764–5769. [in Chinese].
- [23] Ito M, Hiratsuka T, Shibata M. Feature-based visual target following for a nonholonomic wheeled mobile robot with a single camera. 36th Annual Conference on IEEE Industrial Electronics; 2010 Nov 7–10; Glendale, AZ, USA; 2010. p. 2721–2726.
- [24] Jiang N, Lv J, Kobayashi Y, et al. Adaptive image-based visual servoing of nonholonomic mobile robot with

- on-board camera. 2015 IEEE/SICE International Symposium on System Integration (SII); 2015 Dec 11–13; Nagoya, Japan; 2015. p. 983–988.
- [25] Zhang X, Fang Y, Liu X. Adaptive visual servo regulation of mobile robots. *Control Theory Appl.* **2010**;27(9): 1123–1130. [in Chinese].
- [26] Zhang X, Fang Y, Li B, et al. Visual servoing of non-holonomic mobile robots with uncalibrated camera-to-robot parameters. *IEEE Trans Ind Electron.* **2017**;64(1): 390–400.
- [27] Lu Q, Yu L, Zhang D, Zhang X. Simultaneous tracking and regulation visual servoing of wheeled mobile robots with uncalibrated extrinsic parameters. *Int J Syst Sci.* **2018**;49(1):217–229.
- [28] Wang H, Zhu Q. Adaptive output feedback control of stochastic nonholonomic systems with nonlinear parameterization. *Automatica.* **2018**;98:247–255.
- [29] Tian YP, Li S. Exponential stabilization of nonholonomic dynamic systems by smooth time-varying control. *Automatica.* **2002**;38(7):1139–1146.
- [30] Sordalen OJ, Egeland O. Exponential stabilization of non-holonomic chained systems. *IEEE Trans Autom Contr.* **1995**;40(1):35–49.
- [31] Han J. Active disturbance rejection controller and its application. *Control Decis.* **1998**;13(1):19–23. [in Chinese].
- [32] Han J. From pid to active disturbance rejection control. *IEEE Trans Ind Electron.* **2009 March**;56(3):900–906.
- [33] Huang Y, Xue W. Active disturbance rejection control: methodology and theoretical analysis. *ISA Trans.* **2014**;53(4):963–976.
- [34] Guo BZ, Zhao ZL. On the convergence of an extended state observer for nonlinear systems with uncertainty. *Syst Control Lett.* **2011**;60(6):420–430.
- [35] Xue W, Huang Y. Performance analysis of 2-DOF tracking control for a class of nonlinear uncertain systems with discontinuous disturbances. *Int J Robust Nonlinear Control.* **2017**;28(16):1456–1473.
- [36] Hutchinson S, Hager GD, Corke PI. A tutorial on visual servo control. *IEEE Trans Robot Autom.* **1996**;12(5): 651–670.
- [37] Hashimoto K, Noritsugu T. Visual servoing of nonholonomic cart. *IEEE International Conference on Robotics and Automation*; 1997 Apr 20–25; IEEE; 1997. p. 1719–1724.
- [38] ROS. 2016. Available from: <http://wiki.ros.org>.
- [39] Oriolo G, De Luca A, Vendittelli M. WMR control via dynamic feedback linearization: design, implementation, and experimental validation. *IEEE Trans Control Syst Technol.* **2002**;10(6):835–852.

Appendix

Substituting (10), (8) to (9), we obtain

$$J_c = \begin{bmatrix} -\frac{f_u v_1}{c_1} & \frac{u_1 v_1}{c_1} & -f_u - \frac{u_1^2}{f_u} \\ 0 & \frac{v_1^2}{c_1} & -\frac{u_1 v_1}{f_u} \\ -\frac{f_u v_2}{c_2} & \frac{u_2 v_2}{c_2} & -f_u - \frac{u_2^2}{f_u} \\ 0 & \frac{v_2^2}{c_2} & -\frac{u_2 v_2}{f_u} \end{bmatrix}, \quad (A1)$$

where $c_1 = f_v Y_1^*$ and $c_2 = f_v Y_2^*$. Firstly, two vectors are defined for description conciseness as follows:

$$\mathbf{G} = \begin{bmatrix} f_u, \frac{1}{f_u}, -\frac{f_u(a \sin \phi + b \cos \phi)}{c_1}, \\ -\frac{f_u(a \sin \phi + b \cos \phi)}{c_2}, \frac{b \sin \phi - a \cos \phi}{c_1}, \\ \frac{b \sin \phi - a \cos \phi}{c_2}, \frac{f_u \sin \phi}{c_1}, \frac{f_u \sin \phi}{c_2}, \frac{\cos \phi}{c_1}, \frac{\cos \phi}{c_2} \end{bmatrix}^T \in \mathbb{R}^{10} \quad (A2)$$

and

$$\mathbf{F}(\mathbf{p}_c) = \begin{bmatrix} -2l_1 \\ -(l_1(u_1^2 + u_2^2) + l_2(u_1 v_1 + u_2 v_2)) \\ -l_1 v_1 \\ -l_2 v_2 \\ l_1 u_1 v_1 + l_2 v_1^2 \\ l_1 u_2 v_2 + l_2 v_2^2 \\ -2l_5 \\ -(l_3(u_1^2 - u_2^2) - l_4(u_1 v_1 - u_2 v_2)) \\ -(l_5(u_1^2 + u_2^2) + l_6(u_1 v_1 + u_2 v_2)) \\ -(l_3 + l_5)v_1 \\ -(l_5 - l_3)v_2 \\ (l_3 + l_5)u_1 v_1 + (l_6 - l_4)v_1^2 \\ (l_5 - l_3)u_2 v_2 + (l_4 + l_6)v_2^2 \end{bmatrix} \in \mathbb{R}^{12}. \quad (A3)$$

Symbols G_i and F_i are the i th elements of the vectors \mathbf{G} and $\mathbf{F}(\mathbf{p}_c)$. Then cascade multiplying (7), (A1) and (2) with control input, we have

$$\dot{\mathbf{f}} = \mathbf{H}(\mathbf{p}_c) \mathbf{U}_r = \begin{bmatrix} \sum_{i=3}^6 G_{i+4} F_i & \sum_{i=1}^6 G_i F_i \\ \sum_{i=3}^6 G_{i+4} F_{i+6} & \sum_{i=1}^6 G_i F_{i+6} \end{bmatrix} \mathbf{U}_r, \quad (A4)$$

which is exactly the system model (11).